

Application of the Exact Muffin-Tin Orbitals Theory: the Spherical Cell Approximation

L. Vitos¹, H. L. Skriver², B. Johansson¹, J. Kollár³

¹*Condensed Matter Theory Group, Physics Department,
Uppsala University, S-75121 Uppsala, Sweden*

²*Center for Atomic-scale Materials Physics and Department of Physics,
Technical University of Denmark, DK-2800 Lyngby, Denmark*

³*Research Institute for Solid State Physics,
H-1525 Budapest, P.O.Box 49, Hungary*

(8 October 1999)

Abstract

We present a self-consistent electronic structure calculation method based on the *Exact Muffin-Tin Orbitals* (EMTO) Theory developed by O. K. Andersen, O. Jepsen and G. Krier (in *Lectures on Methods of Electronic Structure Calculations*, Ed. by V. Kumar, O.K. Andersen, A. Mookerjee, Word Scientific, 1994 pp. 63-124) and O. K. Andersen, C. Arcangeli, R. W. Tank, T. Saha-Dasgupta, G. Krier, O. Jepsen, and I. Dasgupta, (in *Mat. Res. Soc. Symp. Proc.* **491**, 1998 pp. 3-34). The EMTO Theory can be considered as an *improved screened* KKR (Korringa-Kohn-Rostoker) method which is able to treat large overlapping potential spheres. Within the present implementation of the EMTO Theory the one electron equations are solved exactly using the Green's function formalism, and the Poisson's equation is solved within the *Spherical Cell Approximation* (SCA). To demonstrate the accuracy of the SCA-EMTO method test calculations have been carried out.

I. INTRODUCTION

During the last decades many attempts have been made to develop accurate and at the same time efficient methods for solving the Kohn-Sham equations in an application of the Density Functional Theory for condensed matter. The accuracy of the methods is crucial e.g. when one searches for the answers given by different density functional approximations. The full-potential techniques have been specially designed to fulfill this requirement. Though, in principle, they give highly accurate results, they have their own limitations. In many cases a compromise has been made between the accuracy and efficiency, and methods based on approximate one electron potentials have been developed. The most commonly used muffin tin approach, albeit its mathematical formulation is very elegant, presents a rather poor representation of the exact potential. Though, the *Atomic Sphere Approximation* (ASA) brings a real improvement to the potential, most of the conventional methods based on the ASA use similar approximation to the one electron energies and charge density as well [1]. Therefore, using these methods, reasonably accurate results can only be obtained for close packed systems, and they are not suitable to treat systems of low symmetry. In order to maintain or increase the accuracy different corrections should be included and, therefore, the ASA based methods lose their elegance and efficiency.

A few years ago breakthrough was made by developing the Exact Muffin-Tin Orbitals (EMTO) Theory [2,3]. Within the EMTO Theory the one electron states are calculated exactly for the overlapping muffin-tin potential, while the solution of Poisson's equation can include certain shape approximations, if required. By separating the two approaches used for the potential and one electron states the accuracy can be sustained at a level comparable with that of the full-potential techniques without losing significantly from the efficiency. The EMTO Theory can be considered as an improved screened KKR method [4,5], within that large overlapping potential spheres can be used for accurate representation of the exact one electron potential [3,6].

In this work we present a self-consistent implementation of the EMTO Theory within the *Spherical Cell Approximation* (SCA) for the Poisson's equation. In the first part we review the EMTO Theory [2,3], the definition of the screened spherical waves and the matching equation. Furthermore, we establish the expressions for the number of states and electron density using the Green's function formalism. In the second part of the paper we discuss the impact of the SCA, used for the shape of the Wigner-Seitz cell, on the total charge density and on the overlapping muffin tin potential. Finally, we establish the accuracy of the SCA-EMTO method by performing test calculations for some systems where reliable full-potential data are available. An approximate solution of the kink cancellation equation in order to reduce the number of iterations needed in a self-consistent calculation is presented in the Appendix.

II. OVERVIEW: THE EMTO THEORY

In the following we review the basic concepts of the EMTO Theory developed by O. K. Andersen and co-workers [2,3,7]. Assume that the one-electron Kohn-Sham equations,

$$[-\nabla^2 + v(\mathbf{r})] \Psi_j(\mathbf{r}) = \epsilon_j \Psi_j(\mathbf{r}), \quad (1)$$

are solved within the muffin tin approximation for the effective potential,

$$v(\mathbf{r}) \approx v_0 + \sum_R [v_R(r_R) - v_0], \quad (2)$$

where R runs over the lattice sites. Here and in the following we use the notation $\mathbf{r}_R \equiv \mathbf{r} - \mathbf{R}$ and omit the vector notation for the index R . In (2) v_0 denotes a parameter [7] that reduces to the muffin tin zero in the case of non-overlapping muffin tins. The spherical potentials $v_R(r_R)$ become equal to v_0 outside the potential spheres of radii s_R . These radii can be chosen as the linear overlap between the spheres to be as large as 30 – 40 % [4,3,6]. It has turned out that for a good representation of the real full-potential in terms of overlapping muffin tin wells usually a big overlap is preferred between the potential spheres [6].

In order to solve the Schrödinger equation (1) for the muffin tin potential (2) one chooses different basis functions inside the potential spheres and in the interstitial region. Inside the sphere at \mathbf{R} the partial waves are chosen as the basis function which are defined as the products of the regular solutions of the radial Schrödinger equation,

$$\frac{\partial^2 [r_R \phi_{Rl}(\epsilon, r_R)]}{\partial r_R^2} = \left[\frac{l(l+1)}{r_R^2} + v_R(r_R) - \epsilon \right] r_R \phi_{Rl}(\epsilon, r_R), \quad (3)$$

and the real spherical harmonics, viz.

$$\phi_{RL}(\epsilon, \mathbf{r}_R) = \phi_{Rl}(\epsilon, r_R) Y_L(\hat{r}_R), \quad (4)$$

where $L = (l, m)$. Outside the spheres the so called *screened spherical waves*, $\psi_{RL}^a(\kappa, \mathbf{r}_R)$, are used as basis functions. Therefore, the wave function for the energy ϵ_j can be written as

$$\Psi_j(\mathbf{r}) = \sum_{RL} \phi_{RL}(\epsilon_j, \mathbf{r}_R) \Theta_R(\mathbf{r}_R) u_{RL,j}^a + \sum_{RL} \psi_{RL}^a(\kappa_j, \mathbf{r}_R) [1 - \Theta_R(\mathbf{r}_R)] v_{RL,j}^a. \quad (5)$$

Here $\kappa^2 = \epsilon - v_0$, and in the non-overlapping muffin tins limit it denotes the interstitial one-electron kinetic energy. The $\Theta_R(\mathbf{r}_R)$ is one inside the sphere of radius s_R centered at \mathbf{R} and zero outside. The expansion coefficients $u_{RL,j}^a$ and $v_{RL,j}^a$ as well as the energies ϵ_j are determined from the condition that the wave function $\Psi_j(\mathbf{r})$ and its first derivative should be continuous at the potential spheres. The algebraic formulation of this matching condition in the EMTO formalism is the so the called *kink cancellation equation*, which is equivalent to the KKR (Korringa-Kohn-Rostoker) equation in an arbitrarily screened representation [5].

A. The screened spherical waves

The screened spherical waves can be defined [2] in conjunction with hard spheres centered at all sites \mathbf{R} with radii a_R . They are solutions of the wave equation,

$$\left[\nabla^2 + \kappa^2\right] \psi_{RL}^a(\kappa^2, \mathbf{r}_R) = 0, \quad (6)$$

with the boundary condition that on their own a -spheres they behave like a pure real spherical harmonic, while the $Y_{L'}(\hat{r}_{R'})$ projections on all the other a -spheres, $R' \neq R$, vanish. They form a complete basis set in the "a" interstitial region and may be expressed in terms of the "value", f_{RL}^a , and the "slope", g_{RL}^a , functions [2], whose radial part satisfy the following boundary conditions

$$f_{RL}^a(\kappa, r)|_{a_{RL}} = 1 \quad \text{and} \quad \frac{\partial f_{RL}^a(\kappa, r)}{\partial r}|_{a_{RL}} = 0, \quad (7)$$

$$g_{RL}^a(\kappa, r)|_{a_{RL}} = 0 \quad \text{and} \quad \frac{\partial g_{RL}^a(\kappa, r)}{\partial r}|_{a_{RL}} = \frac{1}{a_{RL}}. \quad (8)$$

These functions may of course be expressed in terms of the usual spherical Bessel and Neumann functions [8]

$$f_{RL}^a(\kappa, r) = j_l(\kappa r) \mathcal{W}_a\{f, \kappa n\} - \kappa n_l(\kappa r) \mathcal{W}_a\{f, j\} \quad (9)$$

and

$$g_{RL}^a(\kappa, r) = j_l(\kappa r) \mathcal{W}_a\{g, \kappa n\} - \kappa n_l(\kappa r) \mathcal{W}_a\{g, j\} \quad (10)$$

since $\mathcal{W}_r\{j, n\} = 1/\kappa$, and therefore satisfy the Wronskian

$$\mathcal{W}_r\{f_{RL}^a, g_{RL}^a\} \equiv r^2 \left[f_l^a(\kappa, r) \frac{\partial g_l^a(\kappa, r)}{\partial r} - \frac{\partial f_l^a(\kappa, r)}{\partial r} g_l^a(\kappa, r) \right] = a_{RL}. \quad (11)$$

The screened spherical wave $\psi_{RL}^a(\kappa^2, \mathbf{r}_R)$ may be expanded in spherical harmonics $Y_{L'}(\hat{r}_{R'})$ about any site \mathbf{R}' , as

$$\psi_{RL}^a(\kappa^2, \mathbf{r}_R) = f_{RL}^a(\kappa, r_R) Y_L(\hat{r}_R) \delta_{RR'} \delta_{LL'} + \sum_{L'} g_{R'L'}^a(\kappa, r_{R'}) Y_{L'}(\hat{r}_{R'}) S_{R'L'RL}^a(\kappa^2), \quad (12)$$

where the expansion coefficients, $S_{R'L'RL}^a(\kappa^2)$, are the elements of the so called *slope matrix*. The slope matrix can be derived from the bare KKR structure constant matrix $B_{R'L',RL}(\kappa)$, by matrix inversion [2]

$$S^a(\kappa^2) = \mathcal{D}\{j(\kappa, a)\} - \frac{1}{a j(\kappa, a)} \left[-B(\kappa) + \kappa \cot \alpha(\kappa) \right]^{-1} \frac{1}{j(\kappa, a)}, \quad (13)$$

where \mathcal{D} denotes the logarithmic derivative, $\mathcal{D}\{j(r)\} \equiv r [\partial j(r)/\partial r] / j(r)$, and for simplicity where we have used matrix notation. We note that this equation is equivalent to Eq. (3.26) from Ref. [2] and Eq. (15) from Ref. [3]. The bare KKR structure constants are defined as the expansion coefficients of the $\kappa n_L(\kappa, \mathbf{r}_R) \equiv \kappa n_l(\kappa r_R) Y_L(\hat{r}_R)$ functions around site R' in terms of the $j_{L'}(\kappa, \mathbf{r}_{R'}) \equiv j_{l'}(\kappa r_{R'}) Y_{L'}(\hat{r}_{R'})$ functions, i.e.

$$\kappa n_L(\kappa, \mathbf{r}_R) = \sum_{L'} j_{L'}(\kappa, \mathbf{r}_{R'}) B_{R'L'RL}(\kappa),$$

with

$$B_{R'L'RL}(\kappa) \equiv 4\pi \sum_{L''} C_{LL'}^{L''} i^{-l+l''-l''} \kappa n_{L''}(\kappa, \mathbf{R}' - \mathbf{R}), \quad (14)$$

and where $C_{LL'}^{L''}$ are the real Gaunt numbers.

For the partial waves explicitly included in the formalism, the *so called low partial waves* with $l \leq l_{low} = 2 - 3$, $\alpha_{Rl}(\kappa)$ are the hard sphere phase shifts given by

$$\cot \alpha_{Rl}(\kappa) = n_l(\kappa a_{Rl}) / j_l(\kappa a_{Rl})$$

and for the remaining Rl -channels, $\alpha_{Rl}(\kappa)$ are the proper phase shifts. For high l 's the latter vanish, and at that point the matrix to be inverted in (13) can be truncated.

When the hard sphere radii, a_R , are properly chosen and κ^2 lies below the bottom of the hard sphere continuum, the screened spherical waves have short range. Therefore, the slope matrix can be calculated in real space and the method is suitable to treat impurities, defects, surfaces, etc. It was shown in Ref. [2] that the shortest range of the screened spherical waves can be achieved for non-overlapping spheres with $a_R \approx 0.5 - 0.85 s_R^i$, depending on the maximal orbital quantum number l of the partial waves explicitly included in the formalism. The s_R^i denotes the inscribed or touching sphere radii. In the KKR community, it is customary to determine the $\alpha_{Rl}(\kappa)$'s as the phase shifts of repulsive potentials.

Because a screened spherical wave has pure (l, m) character only on its own a -sphere, the matching condition in Eq. (5) should be set up at this sphere. The connection onto the potential sphere (s) is done by introducing a free electron solution $\varphi_{Rl}(\epsilon, r_R) Y_L(\hat{r}_R)$ from the potential sphere back to the hard sphere, which joins continuously and differentiable to the partial wave, $\phi_{Rl}(\epsilon, \mathbf{r}_R)$, at s_R and continuously to the screened spherical wave at a_{Rl} . The radial part of this backwards extrapolated free-electron solution, after normalizing it to one at its a -sphere, is given by

$$\varphi_{Rl}^a(\epsilon, r) \equiv \frac{\varphi_{Rl}(\epsilon, r)}{\varphi_{Rl}(\epsilon, a_{Rl})} = f_{Rl}^a(\kappa, r) + g_{Rl}^a(\kappa, r) D_{Rl}^a(\epsilon), \quad (15)$$

where $D_{Rl}^a(\epsilon)$ is the logarithmic derivative of $\varphi_{Rl}(\epsilon, r)$ calculated at the hard sphere a_{Rl} . This can be determined from the matching condition between $\phi_{Rl}(\epsilon, r)$ and $\varphi_{Rl}(\epsilon, r)$ at $r_R = s_R$,

$$D_{Rl}^a(\epsilon) \equiv \mathcal{D}\{\varphi_{Rl}^a(\epsilon, a_{Rl})\} = -\frac{f_{Rl}^a(\kappa, s_R)}{g_{Rl}^a(\kappa, s_R)} \frac{\mathcal{D}\{\phi_{Rl}(\epsilon, s_R)\} - \mathcal{D}\{f_{Rl}^a(\kappa, s_R)\}}{\mathcal{D}\{\phi_{Rl}(\epsilon, s_R)\} - \mathcal{D}\{g_{Rl}^a(\kappa, s_R)\}}. \quad (16)$$

The relation between the values of the free electron function at a and the partial wave at s is

$$\frac{\varphi_{Rl}(\epsilon, a_{Rl})}{\phi_{Rl}(\epsilon, s_R)} = \frac{\varphi_{Rl}(\epsilon, a_{Rl})}{\varphi_{Rl}(\epsilon, s_R)} = \frac{1}{f_{Rl}^a(\kappa, s_R)} \frac{\mathcal{D}\{\phi_{Rl}(\epsilon, s_R)\} - \mathcal{D}\{g_{Rl}^a(\kappa, s_R)\}}{\mathcal{D}\{f_{Rl}^a(\kappa, s_R)\} - \mathcal{D}\{g_{Rl}^a(\kappa, s_R)\}}, \quad (17)$$

In Fig. 1 we have plotted the logarithmic derivative at $a = 0.7 w$, where w denotes the average Wigner-Seitz radius, and the normalization function $\varphi_{Rl}(\epsilon, a_{Rl})$ given in (17) in the case of *fcc* Ga. The logarithmic derivative is a never increasing function of energy and it has a pole above the top of the respective band. Between these poles $D_{Rl}^a(\epsilon)$ is

smooth functions of energy, which varies more slowly than $\mathcal{D}\{\phi_{RL}(\epsilon, s)\}$, because $a < s$. The poles of $D_{RL}^a(\epsilon)$ depend on the representation (a) and they are not related directly to the band structure. The $\varphi_{RL}(\epsilon, a_R)$ from the figure was obtained for partial waves normalized in the w -sphere. It is always a smooth function of the energy and vanishes at the poles of $D_{RL}^a(\epsilon)$.

The slope matrix, Eq. (13), the logarithmic derivative, Eq. (16), and the normalization function, Eq. (17), play a central role in the present implementation of the EMTO Theory.

B. Kink cancellation equation

Using the free electron solutions from (12) and (15) and the partial waves $\phi_{RL}(\epsilon, \mathbf{r}_R)$ we can introduce a complete basis set defined in the whole space. These exact muffin tin orbitals or kinked partial waves may be written in the form

$$\bar{\psi}_{RL}^a(\epsilon, \mathbf{r}_R) = (\phi_{RL}^a(\epsilon, r_R) - \varphi_{RL}^a(\epsilon, r_R)) Y_L(\hat{r}_R) + \psi_{RL}^a(\kappa^2, \mathbf{r}_R), \quad (18)$$

where the radial part of the functions ϕ_{RL}^a and φ_{RL}^a are truncated outside the sphere of radius s_R and outside s_R and inside a_R , respectively. Moreover, the $l \leq l_{low}$ projection of the ψ_{RL}^a function is truncated inside the sphere of radius a_R , while the high- l components penetrate into the hard spheres. The $\bar{\psi}_{RL}^a(\epsilon, \mathbf{r}_R)$ functions are continuous and differentiable in the whole space, except at the hard spheres, where they have non zero kinks. In Eq. (18) the partial waves are renormalized according to Eq. (15)

$$\phi_{RL}^a(\epsilon, r_R) \equiv \frac{\phi_{RL}(\epsilon, r_R)}{\varphi_{RL}(\epsilon, a_R)}. \quad (19)$$

From Eq. (17) and (19) it is immediately seen that the multiplicative normalization of the partial waves does not enter in the expression of the kinked partial wave. Forming a linear combination of the kinked partial waves,

$$\Psi_j(\mathbf{r}) = \sum_{RL} \bar{\psi}_{RL}^a(\epsilon_j, \mathbf{r}_R) v_{RL,j}^a, \quad (20)$$

and asking for the kinks be canceled we arrive to the kink cancellation or screened KKR equations

$$\sum_{RL} K_{R'L'RL}^a(\epsilon_j) v_{RL,j}^a \equiv \sum_{RL} a_{R'} \left[S_{R'L'RL}^a(\kappa_j^2) - \delta_{R'R} \delta_{L'L} D_{RL}^a(\epsilon_j) \right] v_{RL,j}^a = 0 \text{ for all } R'L'. \quad (21)$$

Here we have $l, l' \leq l_{low}$. The solutions of this equation are the one-electron energies and eigenfunctions, which, using Eq. (5) are given by

$$u_{RL,j} = \frac{v_{RL,j}^a}{\varphi_{RL}(\epsilon_j, a_R)}. \quad (22)$$

It is worth to note that in the final expression of the wavefunction $\Psi_j(\mathbf{r})$, Eq. (5), the backwards extrapolated free electron solution does not enter.

In the case of translation symmetry in Eq. (21) R and R' run over the atoms in the primitive cell only, and the slope matrix, and thus the kink matrix $K_{R'L'RL}^a$ as well, depend on the Bloch vector \mathbf{k} from the first Brillouin zone. In Fig. 2 we plotted the diagonal elements of the *fcc* slope matrix (symbols) calculated at the center of the Brillouin zone as a function of the dimensionless energy parameter $(\kappa w)^2$. In this calculation the matrix inversion in (13) was performed in real space for 5 coordination shells plus the central site using the *s*, *p* and *d* orbitals and $0.7w$ for the hard sphere radius. The figure demonstrates the weak and smooth energy dependence of the slope matrix up to the bottom of the continuum, $(\kappa w)^2 \approx 6$. Therefore in the practical solution of the kink cancellation equation (21) the slope matrix can be estimated using a Taylor expansion around a fixed energy κ_0^2 ,

$$S_{R'L'RL}^a(\kappa^2) = S_{R'L'RL}^a(\kappa_0^2) + \frac{1}{1!} \dot{S}_{R'L'RL}^a(\kappa_0^2)(\kappa^2 - \kappa_0^2) + \dots, \quad (23)$$

where the overdot indicates energy derivative. The first and higher order energy derivatives are calculated analytically as described in Ref. [9]. In equation (23) κ^2 is a complex energy not too far from κ_0^2 . In Fig. 2 the solid lines were calculated with a fourth order expansion around $\kappa_0 = 0$. As one can observe, this expansion gives highly accurate energy dependence of the slope matrix over an energy range of approximately $(-1, +1)Ry$.

C. The electron density

In order to construct the new one-electron potential for a self-consistent calculation first we need to construct the electron density given by

$$n(\mathbf{r}) = \sum_j^{\epsilon_j \leq \epsilon_F} |\Psi_j(\mathbf{r})|^2, \quad (24)$$

where the sum runs over the one-electron states below the Fermi level ϵ_F . In the present implementation of the method instead of calculating explicitly the wave functions (5) and performing the summation in Eq. (24) we introduce the path operator $g_{R'L'RL}^a(z, \mathbf{k})$ defined for a complex energy z and Bloch vector \mathbf{k} by

$$\sum_{R''L''} K_{R'L'R''L''}^a(z, \mathbf{k}) g_{R''L''RL}^a(z, \mathbf{k}) = \delta_{R'R} \delta_{L'L}. \quad (25)$$

This function is analytic in the complex plane and it has poles at the one-electron energies along the real axis. Therefore, using the residue theorem, for the total number of electrons we find

$$N(\epsilon_F) = \frac{1}{2\pi i} \oint_{\epsilon_F} \sum_{R'L'RL} \int_{BZ} g_{R'L'RL}^a(z, \mathbf{k}) \dot{K}_{RLR'L'}^a(z, \mathbf{k}) d\mathbf{k} dz, \quad (26)$$

where the first integration is performed on a complex contour and the second one in the first Brillouin zone. The contour is chosen in a way that it cuts the real axis below

the bottom of the valence band and at ϵ_F . In (26) $l, l' \leq l_{low}$. The z dependent partial waves, $\phi_{Rl}(z, r_R)$, and logarithmic derivatives, $D_{Rl}^a(z)$, are obtained by solving Eq. (3) for complex energy. The energy derivative of the kink matrix,

$$\dot{K}_{R'L'RL}^a(z, \mathbf{k}) = a_{R'} \left[\dot{S}_{R'L'RL}^a(z - v_0, \mathbf{k}) - \delta_{R'R} \delta_{L'L} \dot{D}_{RL}^a(z) \right], \quad (27)$$

is calculated by taking the derivatives of Eq. (16) and (23), where the energy derivatives of the basis functions $\{f^a, g^a\}$ are calculated analytically. The energy derivative of the logarithmic derivative function is given by [2]

$$\frac{\partial \mathcal{D}\{\phi_{Rl}(z, s_R)\}}{\partial z} = - \frac{\int_0^{s_R} \phi_{Rl}^2(z, r_R) r_R^2 dr_R}{s_R \phi_{Rl}^2(z, s_R)}. \quad (28)$$

Because the eigenvectors are normalized as (see Ref. [2])

$$\int \Psi_j^*(\mathbf{r}) \Psi_j(\mathbf{r}) d\mathbf{r} = \sum_{R'L'RL} v_{R'L',j}^{a*} \dot{K}_{R'L'RL}^a(\epsilon) v_{RL,j}^a \quad (29)$$

the expression (26) gives the exact number of states at the Fermi level for the muffin tin potential (2). In (29) the negligible terms due to the overlap between s -spheres are omitted [3].

Inside the unit cell at R the electron density in terms of the path operator can be expressed as

$$n(\mathbf{r}_R) = \frac{1}{2\pi i} \oint_{\epsilon_F} \sum_{L'L} Z_{RL'}^a(z, \mathbf{r}_R) \int_{BZ} \tilde{g}_{RL'RL}^a(z, \mathbf{k}) d\mathbf{k} Z_{RL}^a(z, \mathbf{r}_R) dz, \quad (30)$$

where we have introduced the functions

$$Z_{RL}^a(z, \mathbf{r}_R) = \begin{cases} \phi_{Rl}^a(z, r_R) Y_L(\hat{r}_R) & \text{if } l \leq l_{low} \text{ and } r_R \leq s_R \\ \varphi_{Rl}^a(z, r_R) Y_L(\hat{r}_R) & \text{if } l \leq l_{low} \text{ and } r_R > s_R \\ -j_l(z, r_R) Y_L(\hat{r}_R) & \text{if } l > l_{low} \text{ for all } r_R \end{cases}, \quad (31)$$

and where the sums over l' and l include the high- l terms as well. These functions are equivalent to the scattering solutions of Faulkner and Stocks [10]. In Eq. (30) we have introduced the following matrix

$$\tilde{g}_{RL'RL}^a(z, \mathbf{k}) \equiv \begin{cases} g_{RL'RL}^a(z, \mathbf{k}) & \text{if } l, l' \leq l_{low} \\ \sum_{R''L''} g_{RL'R''L''}^a(z, \mathbf{k}) S_{R''L''RL}^a(z, \mathbf{k}) & \text{if } l' \leq l_{low} \text{ and } l > l_{low} \\ \sum_{R''L''} S_{RL'R''L''}^a(z, \mathbf{k}) g_{R''L''RL}^a(z, \mathbf{k}) & \text{if } l' > l_{low} \text{ and } l \leq l_{low} \\ \sum_{R''L''} \sum_{R'''L'''} S_{RL'R''L''}^a(z, \mathbf{k}) \\ \times g_{R''L''R'''L'''}^a(z, \mathbf{k}) S_{R'''L'''RL}^a(z, \mathbf{k}) & \text{if } l', l > l_{low} \end{cases} \quad (32)$$

where the high-low and the low-high subblocks of the slope matrix are calculated by the usual blowing-up technique [11].

In principle Eq. (26) and (30) give the exact number of states and electron density. However, in some cases, like for the metals from the *IIB* and *III-V*A groups, where one of the d bands is completely filled, around the top of this band the normalization function (17) goes through zero. This happens, for example, in the case of *fcc* Ga

around the top of the $3d$ band, as it can be seen from Fig. 1. For this energy not only the logarithmic derivative but also its energy derivative \dot{D}_{Rl}^a , appearing in the diagonal of the $\dot{K}_{R'l'RL}^a$ matrix, has poles. In order to cancel these nonphysical poles we rewrite the expression for the number of states as

$$N(\epsilon_F) = \frac{1}{2\pi i} \oint_{\epsilon_F} G(z) dz, \quad (33)$$

where

$$G(z) \equiv \sum_{R'l'RL} \int_{BZ} g_{R'l'RL}^a(z, \mathbf{k}) \dot{K}_{RLR'l'}^a(z, \mathbf{k}) d\mathbf{k} - \sum_{RL} \left[\frac{\dot{D}_{Rl}^a(z)}{D_{Rl}^a(z)} - \sum_{\epsilon_{Rl}^D} \frac{1}{z - \epsilon_{Rl}^D} \right], \quad (34)$$

with $l, l' \leq l_{low}$, and that of the electron density as

$$\begin{aligned} n(\mathbf{r}_R) &= \frac{1}{2\pi i} \oint_{\epsilon_F} \sum_{L'l} Z_{RL'l}^a(z, \mathbf{r}_R) \int_{BZ} \tilde{g}_{RL'l}^a(z, \mathbf{k}) d\mathbf{k} Z_{RL}^a(z, \mathbf{r}_R) dz \\ &+ \frac{1}{2\pi i} \oint_{\epsilon_F} \sum_L \frac{Z_{RL}^{a2}(z, \mathbf{r}_R)}{a_R D_{Rl}^a(z)} dz - \sum_L \sum_{\epsilon_{Rl}^D} \frac{Z_{RL}^{a2}(\epsilon_{Rl}^D, \mathbf{r}_R)}{a_R \dot{D}_{Rl}^a(\epsilon_{Rl}^D)}, \end{aligned} \quad (35)$$

where ϵ_{Rl}^D are the zeros of the logarithmic derivative function, $D_{Rl}^a(\epsilon)$. Because the logarithmic derivative is a smooth decreasing function of energy ϵ_{Rl}^D 's can be easily determined with high accuracy. The second and third terms from the right hand side of (35) are included only for $l \leq l_{low}$. Using the fact that the residuum of the $1/D_{Rl}^a$ around ϵ_{Rl}^D is $1/\dot{D}_{Rl}^a$, it is easy to show that the poles of $\dot{D}_{Rl}^a(z)$ and those of $1/\varphi_{Rl}(z, a_R)^2$ are canceled out in Eqs. (34) and (35).

From the electron density (35) we determine the overlapping muffin tin wells and repeat the iterations until self consistency, of the total energy for example, is achieved. In the present implementation of the EMTO Theory the solution of the Poisson's equation involves the SCA for the shape of the Wigner-Seitz cell, therefore, the construction of the muffin tin potential will be discussed only within this context.

III. THE SCA-EMTO METHOD

Equations (21) and (33-35), derived in the previous section, constitute the basis of the present method. In order to perform a self-consistent calculation one constructs the electron density from the solutions of the kink cancellation equation and calculates the new one-electron potential. In this section we describe these steps using the SCA for the shape of the Wigner-Seitz cell.

In the SCA, for solving the Poisson's equation, we substitute the Wigner-Seitz cells by spherical cells with volumes equal to the volumes of the real cells. If Ω_R denotes the volume of the Wigner-Seitz cell (Voronoi polyhedron) centered at \mathbf{R} we have $\Omega_R = \Omega_{w_R} \equiv \frac{4\pi}{3} w_R^3$, where w_R is the atomic sphere radius. Thus within the SCA, like in the conventional ASA, the whole space is "covered" by the Ω_{w_R} spheres.

A. The SCA charge density

During the self-consistent calculation the Fermi level of a N electron system is determined by solving the $N(\epsilon_F) = N$ equation, where $N(\epsilon_F)$ is given in (33). For this ϵ_F the electron density is constructed from Eq. (35). Due to the normalization (29) the so constructed density is exactly normalized within the unit cell but not within the SCA spheres of volumes Ω_{w_R} . Therefore, in order to solve the Poisson's equation within the SCA we have to renormalize the total density inside the spheres. In the present implementation of the method this is realized by

$$n^{SCA}(\mathbf{r}_R) = n(\mathbf{r}_R) + aY_{00}(\hat{\mathbf{r}}_R), \quad (36)$$

where the site independent a constant is determined from the condition of the charge neutrality within the whole unit cell

$$\sum_R \int_{\Omega_{w_R}} n^{SCA}(\mathbf{r}_R) d\mathbf{r}_R = \sum_R Z_R. \quad (37)$$

Here Z_R denotes the nuclear charge at R . The sum runs over the atoms from the unit cell, and the integrals are performed inside the SCA spheres. Throughout this section the charge density is normalized within the SCA spheres according to (36) and (37), however, for the sake of simplicity we neglect the *SCA* index for the $n^{SCA}(\mathbf{r})$.

B. The SCA muffin tin potential

The spherical symmetric potentials, $v_R(r_R)$, that enter in Eq. (3) have to be chosen in a way that, together with the parameter v_0 , to give the best approximation to the full potential $v(\mathbf{r})$. The original idea in Ref. [7] is to minimize the mean of the squared deviation between the left and the right hand side of Eq. (2). This leads to a set of integral or differential equations for $v_R(r_R)$ and v_0 . In the non-overlapping muffin tins case the equation for $v_R(r_R)$ reduce to the well known expression

$$v_R(r_R) = \frac{1}{4\pi} \int v(\mathbf{r}) d\hat{\mathbf{r}}_R, \quad (38)$$

and v_0 reduces to the muffin tin zero, i.e. to the average of the full potential calculated in the interstitial region,

$$\Omega^I \equiv \Omega - \sum_R V_R \equiv \Omega - \sum_R \frac{4\pi}{3} s_R^3,$$

where Ω is the volume of the region where the approximation (2) is valid (unit cell), and V_R denotes the volume of the potential sphere.

In the overlapping muffin tins case the equation for the v_0 can be written in the following simple form [7]

$$\sum_R \frac{4\pi}{\Omega} \int_0^{s_R} [v_R(r_R) - v_0] r_R^2 dr + v_0 = \frac{1}{\Omega} \int_{\Omega} v(\mathbf{r}) d\mathbf{r}, \quad (39)$$

while the equation for $v_R(r_R)$ involves terms coming from the overlapping region, and which give rise to kinks of $v_R(r_R)$ when r_R touches other muffin tin spheres. In the present implementation of the method, instead of solving the $v_R(r_R)$ equations, we all the time, for non-overlapping and for overlapping muffin tin wells as well, fix the $v_R(r_R)$ functions to the spherical average of the full potential given by (38). In this case from Eq. (39) we get the expression for the v_0 as

$$v_0 = \frac{1}{\Omega - \sum_R V_R} \left[\int_{\Omega} v(\mathbf{r}) d\mathbf{r} - \sum_R \int_{V_R} v(\mathbf{r}) d\mathbf{r} \right], \quad (40)$$

or

$$v_0 = \frac{\sum_R \left[\int_{\Omega_R^I} v(\mathbf{r}) d\mathbf{r} - \int_{\Omega_R^{ov}} v(\mathbf{r}) d\mathbf{r} \right]}{\sum_R [\Omega_R^I - \Omega_R^{ov}]}, \quad (41)$$

where Ω_R^I is the real interstitial within a Wigner-Seitz cell centered at R with volume Ω_R , and Ω_R^{ov} is that part of the potential sphere that is outside of the cell Ω_R , i.e.

$$\Omega \equiv \sum_R \Omega_R \quad \text{and} \quad \Omega_R^I - \Omega_R^{ov} \equiv \Omega_R - V_R. \quad (42)$$

Eq. (41) assumes the knowledge of the full potential $v(\mathbf{r})$ in Ω_R^I and Ω_R^{ov} regions. However, the time consuming calculation of the full potential can be avoided by using the SCA for the unit cell. In the non-overlapping SCA case, i.e. $s_R < w_R$, we have

$$\Omega_R^I - \Omega_R^{ov} = 4\pi \int_{s_R}^{w_R} r_R^2 dr_R,$$

and

$$\int_{\Omega_R^I} v(\mathbf{r}) d\mathbf{r} - \int_{\Omega_R^{ov}} v(\mathbf{r}) d\mathbf{r} = \int_{s_R}^{w_R} \left[\int v(\mathbf{r}) d\hat{\mathbf{r}}_R \right] r_R^2 dr_R, \quad (43)$$

while for the overlapping SCA case, i.e. $s_R > w_R$, we have

$$\Omega_R^I - \Omega_R^{ov} = -4\pi \int_{w_R}^{s_R} r_R^2 dr_R,$$

and

$$\int_{\Omega_R^I} v(\mathbf{r}) d\mathbf{r} - \int_{\Omega_R^{ov}} v(\mathbf{r}) d\mathbf{r} = - \int_{w_R}^{s_R} \left[\int v(\mathbf{r}) d\hat{\mathbf{r}}_R \right] r_R^2 dr_R. \quad (44)$$

From these equations we get the expression for the parameter v_0 valid within the SCA

$$v_0 = \sum_R \int_{s_R}^{w_R} r_R^2 \left[\int v(\mathbf{r}) d\hat{\mathbf{r}}_R \right] dr_R / \sum_R W_R \quad (45)$$

where $W_R \equiv 4\pi(w_R^3 - s_R^3)/3$. Therefore both of the $v_R(r_R)$ function and the v_0 parameter are given in terms of the spherical symmetric part of the full potential.

The many-body part, $\mu_{xc}[n(\mathbf{r})]$, of the one-electron effective potential,

$$v(\mathbf{r}) = v^C(\mathbf{r}) + \mu_{xc}[n(\mathbf{r})], \quad (46)$$

is calculated within the local density or generalized gradient approximation, while the electrostatic part is derived solving the Poisson's equation,

$$\nabla^2 v^C(\mathbf{r}) = -8\pi \left[n(\mathbf{r}) - \sum_R Z_R \delta(r_R) \right], \quad (47)$$

for the electronic and nuclear charge densities. The electrostatic potential can be divided into intercell and intercell component. The spherical symmetric part of the intercell or Madelung potential is given by

$$v_R^M(r_R) = \frac{1}{w} \sum_{R'L'} M_{RLR'L'} Q_{R'L'} \text{ with } L = (0, 0), \quad (48)$$

where $M_{RLR'L'}$ is the Madelung matrix, which can be evaluated by the usual Ewald technique, and

$$Q_{RL} = \frac{\sqrt{4\pi}}{2l+1} \int_{\Omega_{w_R}} \left(\frac{r_R}{w} \right)^l \left[n_R(\mathbf{r}_R) - Z_R \delta(r_R) \right] Y_L(\hat{r}_R) d\mathbf{r}_R. \quad (49)$$

The Hartree part of the intracell Coulomb potential can be obtained as the solution of the Poisson's equation using the proper boundary condition at the atomic sphere radius. Alternatively, this term is given by

$$v_R^I(r_R) = \begin{cases} 8\pi \left[\frac{1}{r_R} \int_0^{r_R} r_R'^2 n_R(r_R') dr_R' + \int_{r_R}^{w_R} r_R' n_R(r_R') dr_R' \right] & \text{for } r_R \leq w_R \\ 8\pi \frac{1}{r_R} \int_0^{w_R} r_R'^2 n_R(r_R') dr_R' & \text{for } r_R > w_R \end{cases}, \quad (50)$$

that is valid inside the potential sphere s_R , for $s_R \geq w_R$ as well as for $s_R < w_R$. The total potential within the potential sphere is obtained as the sum of Eq. (48), (50), the Coulomb potential of the nucleus and the spherical symmetric exchange-correlation potential, namely

$$v_R(r_R) = v_R^M + v_R^I(r_R) - \frac{2Z_R}{r_R} + \mu_{xc}(r_R). \quad (51)$$

If the spherical symmetric part of the exchange-correlation potential is approximated by $\mu_{xcR}[n_R(r_R)]$ besides the higher order multipole moments from (48), which in many cases can be neglected, all of the potential components from (51) depend only on the spherical symmetric density $n_R(r_R)$.

Within the SCA-EMTO method the atomic and potential spheres can be and usually they are chosen differently. The sizes of the atomic spheres, w_R , are fixed by the volume, and the ratio between them should be chosen in a way that minimizes the errors coming from approximate solution of the Poisson's equation. We have found that the best representation of the potential can be achieved by choosing the potential sphere radii, s_R , larger or equal with the atomic sphere radii. For an optimal choice of the potential spheres the potentials at s_R should be the same, i.e. $v_R(s_R) \approx \text{constant}$ for each R , and this *constant* should have the maximum possible value for linear overlaps below 30 – 40%.

IV. APPLICATIONS: TEST CALCULATIONS

In this section we present a few applications of the SCA-EMTO method. We chose particular systems where the conventional ASA based methods failed and the inclusion of the correction terms or of the exact potential seemed to be unavoidable. First we describe the most important numerical details and after we analyze the present results comparing to the available full-potential calculations.

A. Numerical details

The hard sphere radii are chosen at $a_R = 0.7w$. In the matrix inversion from Eq. (13) we include 79 sites in the case of *fcc*-based structures (*fcc*, $L1_2$ and $L1_0$), and 89 sites in the case of *bcc*-based structures (*bcc*, $B2$ and $B32$). The Taylor expansion of the slope matrix is carried out for $\kappa_0 = 0$ and includes terms up to the fourth to sixth order energy derivative.

The path operator is calculated for 16 – 32 complex energy points, depending on the band structure, distributed exponentially on a semi-circular contour. The k -point sampling is performed on a uniform grid in the 3D Brillouin zones. All the calculations are scalar-relativistic and employ the frozen-core approximation. The basis set include s , p and d orbitals and the valence electrons are treated self-consistently within the local density approximation to density functional theory using the Ceperley and Alder [12] exchange-correlation functional and parametrized by Perdew and Wang [13]. The atomic sphere radii, w_R -s, are chosen in a way that the atomic spheres should have the same volumes as the corresponding Voronoi polyhedra. The electrostatic and exchange-correlation contribution to the total energy is calculated within the SCA as described, for example, in Refs. [14,15]. The kinetic energy is given by

$$T^{SCA} = \frac{1}{2\pi i} \oint_{\epsilon_F} zG(z)dz - \sum_R \int_0^{w_R} v_R(r_R)n_R(r_R)r_R^2 dr_R, \quad (52)$$

where the first term from the right hand side is the sum of the one electron energies and $G(z)$ is given in (34).

B. Results

Before starting on the evaluation of the results we address the question of the accuracy of the Taylor expansion for the slope matrix, Eq. (23). In Fig. 3 the total energy of *fcc* Cu is shown for different number of terms included in the Taylor expansion. The inclusion of the fourth order energy derivative term changes the total energy by 1.13 mRy. The effect of the fifth order term is already less than 0.2 mRy and that of the sixth order term is about 0.04 mRy. Therefore, we conclude that for a reasonable accuracy it is sufficient to include five terms in the expansion of the slope matrix, viz. up to the fourth order energy derivatives. In the case of open structures, wide energy bands or semicore states, however, more terms should be included [16].

The variations of the SCA-EMTO total energy with the potential sphere radius for *fcc* and *bcc* Cu are shown on Fig. 4. For this test calculation the total potential from (45) was weighted by the valence part of the total density according to

$$v_0 = \frac{\sum_R \int_{s_R}^{w_R} r_R^2 [\int n(\mathbf{r})v(\mathbf{r})d\hat{\mathbf{r}}_R] dr_R}{\sum_R \int_{s_R}^{w_R} r_R^2 [\int n(\mathbf{r})d\hat{\mathbf{r}}_R] dr_R}, \quad (53)$$

and the cut-off in (35) for the spherical part of the total density was $l_{max} = l'_{max} = 8$. The inscribed sphere radii are $s_{fcc}^i = 0.91w_{fcc}$ and $s_{bcc}^i = 0.88w_{bcc}$, where the theoretical atomic sphere radii, w_{fcc} and w_{bcc} are shown on the figure. The total energy in both of the *fcc* and *bcc* structures beginning from $s \approx 0.80w$ becomes almost flat with a negligible slope up to $s \approx 1.20w$, which means about 32 – 36% linear overlap for the *fcc* and *bcc* structures, respectively. For $s > 0.80w$ the further increase of the potential sphere radius has little effect on the energy, that means the potential in the corners of the Wigner-Seitz cell is, with a very good approximation, constant. However, for big overlaps, $s > 1.20w$, the errors coming from the overlap region, and neglected in the kink-cancellation equation and in the charge density as well, become important [3].

There is a comprehensive study of the structural stability of the transition metals done either by full-potential or by muffin-tin or ASA based methods. In the latter case correction terms are needed [17] for calculation of the accurate total energies. The conventional ASA without correction terms gives, for example, with about 2 mRy lower total energy for the Cu in the *bcc* phase than in the *fcc* phase. This underestimation of the *bcc* total energy is due to the incorrect kinetic energy term, and the inclusion of the exact Hartree energy would lower even more the *bcc* energy. From a more sophisticated full-potential method [18] a structural energy difference of $E_{bcc} - E_{fcc} \approx 0.5$ mRy was obtained. This number should be compared with our results of 0.4 mRy from Fig. 4. One should note that this difference is almost constant for a wide range of linear overlap.

The second example is the binary $\text{Li}_x\text{Al}_{1-x}$ ordered compound in different phases. There are two reasons of this choice: i) this system is very well studied through accurate full-potential calculations [19,20], and ii) most of the experimentally observed interesting trends, the contraction of the volume of the Al-based alloys, the asymmetric heats of formation with respect to the equiatomic concentration etc., can not be reproduced by an ordinary spherically symmetric calculation. Besides the three different compositions, $x = 0.25, 0.50, 0.75$, we consider the pure Al and Li limits in *fcc* and *bcc* phases as well. For $x = 0.25$ and 0.75 the calculations were performed only for the $L1_2$ structure, while for $x = 0.50$ we considered three different structures: $L1_0, B2$ and $B32$.

In Fig. 5 the charge density contour plots are shown for pure *fcc* Al, and Al_3Li in $L1_0$ structure, as calculated from Eq. (35) using s, p, d basis set, and the maximum orbital quantum number l' included in (12) was 10. The agreement between these plots and those from Ref. [21] is very good.

The calculated equilibrium Wigner-Seitz radii and the bulk moduli are tabulated in Table I and plotted in Figs. 6 and 7. In the case of pure Al and Li the structure energy differences and in the case of compounds the heats of formation are included in the Table and plotted in Fig. 8. The heat of formation is defined as

$$\Delta H \equiv E_{\text{Li}_x\text{Al}_{1-x}} - x E_{\text{Li}} - (1 - x) E_{\text{Al}}, \quad (54)$$

where all the energies are obtained for the proper equilibrium volume and they are expressed per atom. In Figs. 5-7 and Table I the full-potential values from Ref. [20] are also included.

The mean deviations between the present and the full-potential results for the equilibrium radii, bulk moduli and heats of formations are 9.8%, 7.5% and 17%, respectively. Taking into account the minor discrepancies between the numerical details used in the calculations, for example the exchange-correlation functional, the way the core electrons were treated etc., and the fact that the full-potential methods have their own error limits as well, we can conclude that the agreement between the two sets of results is very good. One should appreciate how well the trends obtained in the full-potential calculation are reproduced by the present method.

V. CONCLUSIONS

We have presented a self-consistent implementation based on the Green's function technique of the Exact Muffin-Tin Orbitals Theory, developed by O.K. Andersen *et al.* The accuracy of the present implementation was tested on different systems, where we have found a good agreement between the present results and the results obtained by full-potential techniques. In order to gain some experience about the efficiency of the present method we compare the CPU times of a self-consistent calculation of the tight-binding ASA-LMTO method [11], based also on the Green's function technique, and that of the SCA-EMTO method. We found that the present implementation of the SCA-EMTO method needs with about 3 times larger CPU time than the tight-binding ASA-LMTO method.

Finally we remark that if the radii of the potential spheres are chosen to be equal with the radii of the atomic spheres, i.e. $w_r = s_R$, the SCA-EMTO method can be considered as an ASA based Green's function technique that involves the so called *combined correction* term [22]. It gives exact one electron energies and charge densities for the optimized overlapping muffin tin wells. The natural extension of the present SCA-EMTO method to compute the total energies from the output total charge density via the Full Charge Density technique [23,24] is in progress.

ACKNOWLEDGMENTS

L.V. acknowledges the interesting and helpful discussions with Prof. O. K. Andersen, the assistance from Drs. C. Arcangeli and R. W. Tank, and the hospitality of the Max-Planck Institute from Stuttgart where the first part of this work was performed. Thanks are also due to Dr. A. V. Ruban for his valuable observations. The Swedish Natural Science Research Council, the Swedish Foundation for Strategic Research and Royal Swedish Academy of Sciences are acknowledged for financial support. Center for Atomic-scale Materials Physics is sponsored by the Danish National Research Foundation. Part of this work was supported by the research project OTKA 023390 of the Hungarian Scientific Research Fund.

VI. APPENDIX

During the self-consistent procedure the Eq. (25), (33), (35) and (51) are solved iteratively. In order to construct the electron density (35), as the input for the next iteration, we have to invert the kink matrix for each complex energy z along the contour and for each Bloch vector \mathbf{k} from the Brillouin zone. For a reasonably high accuracy we need at least a few hundreds of Bloch vectors in the irreducible part of the Brillouin zone, therefore this solution means the most time-consuming step of the self-consistent procedure. Here we apply a similar "two-step" scheme introduced in Ref. [25] in order to reduce the number of time-consuming iterations. Within this scheme after each iteration an approximate charge self-consistency is achieved by solving self-consistently the following equation written for the \mathbf{k} -integrated path operator

$$g^a(z) = \left[1 + g^{a0}(z) \left(D^{a0}(z) - D^a(z) \right) \right]^{-1} g^{a0}(z), \quad (55)$$

where where the index 0 denotes quantities obtained from the previous iteration, and which are kept fixed during the solution of Eq. (55).

In the expression for the number of state (33), we need the \mathbf{k} -integrated trace of the product between the path operator and the energy derivative of the kink matrix, therefore, a similar equation to (55) has to be established for the quantity

$$G_{R'L'RL}^a(z) \equiv \int_{BZ} g_{R'L'RL}^a(z, \mathbf{k}) \dot{K}_{RLR'L'}^a(z, \mathbf{k}) d\mathbf{k}. \quad (56)$$

Using the definition of the kink matrix after some manipulations we arrive to the equation

$$G_{R'L'RL}^a(z) = g_{R'L'RL}^a(z) \left[\frac{G_{R'L'RL}^{a0}(z)}{g_{R'L'RL}^{a0}(z)} + \delta_{R'R} \delta_{L'L} a_R \left(\dot{D}_{Rl}^{a0}(z) - \dot{D}_{Rl}^a(z) \right) \right]. \quad (57)$$

It is worth to note that in this expression we do not have matrix multiplication. Finally we mention that as soon as the self-consistency is achieved, i.e.

$$D_{Rl}^a(z) \rightarrow D_{Rl}^{a0}(z) \quad \text{and} \quad \dot{D}_{Rl}^a(z) \rightarrow \dot{D}_{Rl}^{a0}(z), \quad (58)$$

both equations, (55) and (57), become exact.

REFERENCES

- [1] M. Asato, A. Settels, T. Hoshino, T. Asada, S. Blügel, R. Zeller, and P. H. Dederichs, *Phys. Rev. B* **60**, 5202 (1999).
- [2] O. K. Andersen, O. Jepsen, and G. Krier, in *Lectures on Methods of Electronic Structure Calculations*, edited by V. Kumar, O. K. Andersen, and A. Mookerjee, World Scientific Publishing Co., Singapore, pp. 63-124 (1994).
- [3] O. K. Andersen, C. Arcangeli, R. W. Tank, T. Saha-Dasgupta, G. Krier, O. Jepsen, and I. Dasgupta, in *Mat. Res. Soc. Symp. Proc.* **491**, pp. 3-34 (1998).
- [4] O. K. Andersen, A.V. Postnikov, and S.Yu. Savrasov, in *Applications of Multiple Scattering Theory in Materials Science*, edited by W.H. Butler, P.H. Dederichs, A. Gonis, and R.L. Weaver, Materials Research Society, Pittsburgh, PA, (1992).
- [5] L. Szunyogh, B. Újfalussy, P. Weinberger, and J. Kollár, *Phys. Rev. B* **49**, 2721 (1994).
- [6] C. Arcangeli, O.K. Andersen and R.W. Tank (unpublished).
- [7] O.K. Andersen and C. Arcangeli (unpublished).
- [8] *Handbook of Mathematical Functions*, edited by M. Abramowitz and I. A. Stegun, Dover Publications, Inc., New York (1970).
- [9] R. Tank, O.K. Andersen, G. Krier, C. Arcangeli and O. Jepsen (unpublished).
- [10] J.S.Faulkner and G.M. Stocks, *Phys. Rev. B* **21**, 3222 (1980).
- [11] O. K. Andersen, O. Jepsen, and D. Glötzel, in *Highlights of Condensed-Matter Theory*, edited by F. Bassani, F. Fumi, and M. P. Tosi, North-Holland, New York, (1985).
- [12] D. M. Ceperley and B. J. Alder, *Phys. Rev. Lett.* **45**, 566 (1980).
- [13] J. Perdew and Y. Wang, *Phys. Rev. B* **45**, 13244 (1992).
- [14] L. Vitos, J. Kollár, and H. L. Skriver, *Phys. Rev. B* **49**, 16694 (1994).
- [15] H.L. Skriver, *The LMTO Method* (Springer-Verlag, Berlin, 1984).
- [16] L. Vitos (unpublished).
- [17] H.L. Skriver, *Phys. Rev. B* **31**, 1909 (1985).
- [18] T. Kraft, P. M. Marcus, M. Methfessel, and M. Sheffler, *Phys. Rev. B* **48**, 5886 (1993).
- [19] X. Q. Guo, R. Podloucky, and A. J. Freeman, *Phys. Rev. B* **40**, 2793 (1989).
- [20] M. Sluiter, D. de Fontaine, X. Q. Guo, R. Podloucky, and A. J. Freeman, *Phys. Rev. B* **42**, 10460 (1990).
- [21] X. Q. Guo, R. Podloucky, Jian-hua Xu, and A. J. Freeman, *Phys. Rev. B* **41**, 12432 (1990).
- [22] O.K. Andersen, O. Jepsen and M. Sob, in *Electronic Band Structure and its Applications*, ed. M. Yussouff Springer Lecture Notes, (1987).
- [23] L. Vitos, J. Kollár, and H. L. Skriver, *Phys. Rev. B* **55**, 13521 (1997).
- [24] J. Kollár, L. Vitos and H.L. Skriver in *Lecture Notes in Physics*, Springer Series (1999).
- [25] I. A. Abrikosov, S.I. Simak, B. Johansson, A.V. Ruban, and H.L. Skriver, *Phys. Rev. B* **56**, 9319 (1997).
- [26] D. A. Young, *Phase Diagrams of the Elements* (University of California Press, Berkeley, 1991)
- [27] J. M. Sanchez and C. H. Lin, *Phys. Rev. B* **30**, 1448 (1984).

- [28] W. Mueller, E. Bubeck, and V. Gerold, *Proceedings of the 3rd International Conference on Aluminium-Lithium Alloys*, ed. C. Baker, P. J. Gregson, S. J. Harris, and C. J. Peel, TMS-AIME, London, (1986).
- [29] E. A. Brandes, *Smithells Metals Reference Book*, 6th ed., Butterworths, Boston, MA, (1983).
- [30] I. Barin, O. Knacke, and O. Kubaschewski, *Thermochemical Properties of Inorganic Substances*, Springer, Berlin, (1977).

TABLES

TABLE I. The theoretical atomic radii, bulk moduli, heats of formation and *fcc-bcc* structure energy differences of the ordered AlLi compounds, and pure Al and Li. The present SCA-EMTO results are compared to the full-potential FLAPW results, and to the experimental data.

Structure			Present calculation	Full-potential ¹	Experimental
<i>Al₃Li</i>	<i>L1₂</i>	S(Bohr)	2.904	2.935	2.934 ³
		B(GPa)	74.27	70.31	66.0 ⁴
		ΔH (mRy)	-8.21	-8.3	
<i>AlLi</i>	<i>L1₀</i>	S(Bohr)	2.881	2.917	
		B(GPa)	51.04	50.41	
		ΔH (mRy)	-11.53	-10.25	
<i>AlLi</i>	<i>B2</i>	S(Bohr)	2.837	2.876	
		B(GPa)	55.86	42.09	
		ΔH (mRy)	-13.94	-10.45	
<i>AlLi</i>	<i>B32</i>	S(Bohr)	2.863	2.910	2.928 ⁵
		B(GPa)	59.91	57.75	
		ΔH (mRy)	-21.69	-16.60	-18.5 ⁶
<i>AlLi₃</i>	<i>L1₂</i>	S(Bohr)	2.932	2.965	
		B(GPa)	31.45	28.37	
		ΔH (mRy)	-6.71	-5.0	
Al	fcc	S(Bohr)	2.920	2.946	2.991 ²
		B(GPa)	91.76	82.20	72.8 ²
		$E^{bcc} - E^{fcc}$ (mRy)	2.90	4.59	
Al	bcc	S(Bohr)	2.930	2.951	
		B(GPa)	84.46	84.18	
Li	fcc	S(Bohr)	3.112	3.124	
		B(GPa)	15.47	13.64	
		$E^{bcc} - E^{fcc}$ (mRy)	0.29	0.50	
Li	bcc	S(Bohr)	3.117	3.128	3.237 ²
		B(GPa)	15.64	15.25	12.6 ²

¹ FLAPW calculation, Ref. [20]; ² Experimental, Ref. [26];

³ Experimental, Ref. [27]; ⁴ Experimental, Ref. [28];

⁵ Experimental, Ref. [29]; ⁶ Experimental, Ref. [30].

FIGURES

FIG. 1. The energy dependence of the logarithmic derivative $D_{RI}^a(\epsilon)$ (solid line), and normalization function $\varphi_{RI}(\epsilon, a_R)$ (dashed line) for the *fcc* Ga.

FIG. 2. The diagonal elements of the *fcc* slope matrix in the $\mathbf{k} = (0, 0, 0)$ point from the Brillouin zone versus $(\kappa w)^2$. The numbers in parenthesis denote the (l, m) quantum numbers. The Taylor expansion included terms up to the 4th order energy derivative.

FIG. 3. Self-consistent SCA-EMTO total energy of *fcc* Cu for different number of terms included in the Taylor expansion for the slope matrix, Eq. (23).

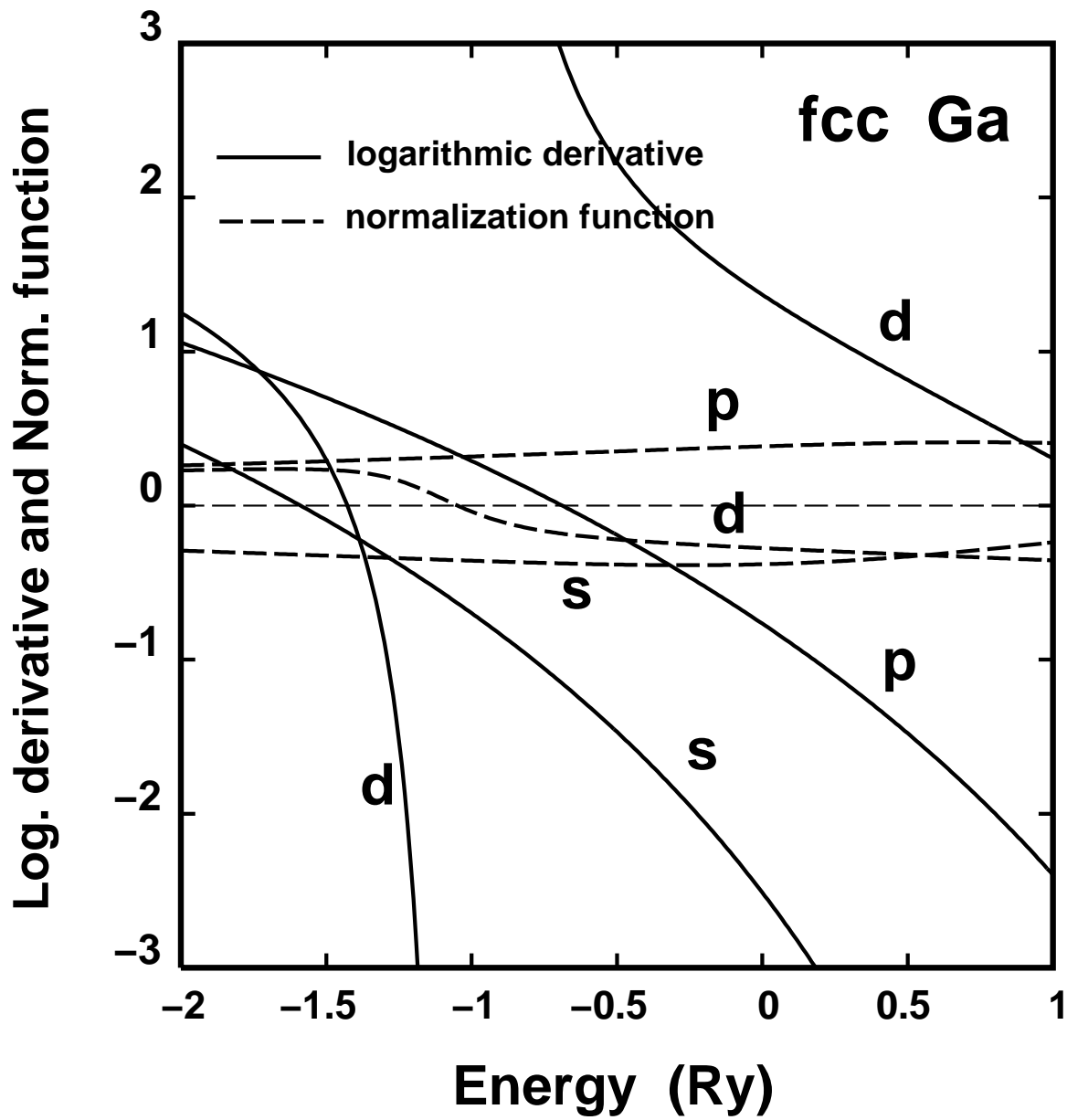
FIG. 4. Total energy versus potential sphere radius, s , for the *fcc* and *bcc* Cu. The calculations were done at the theoretical equilibrium atomic sphere radii shown in the figure.

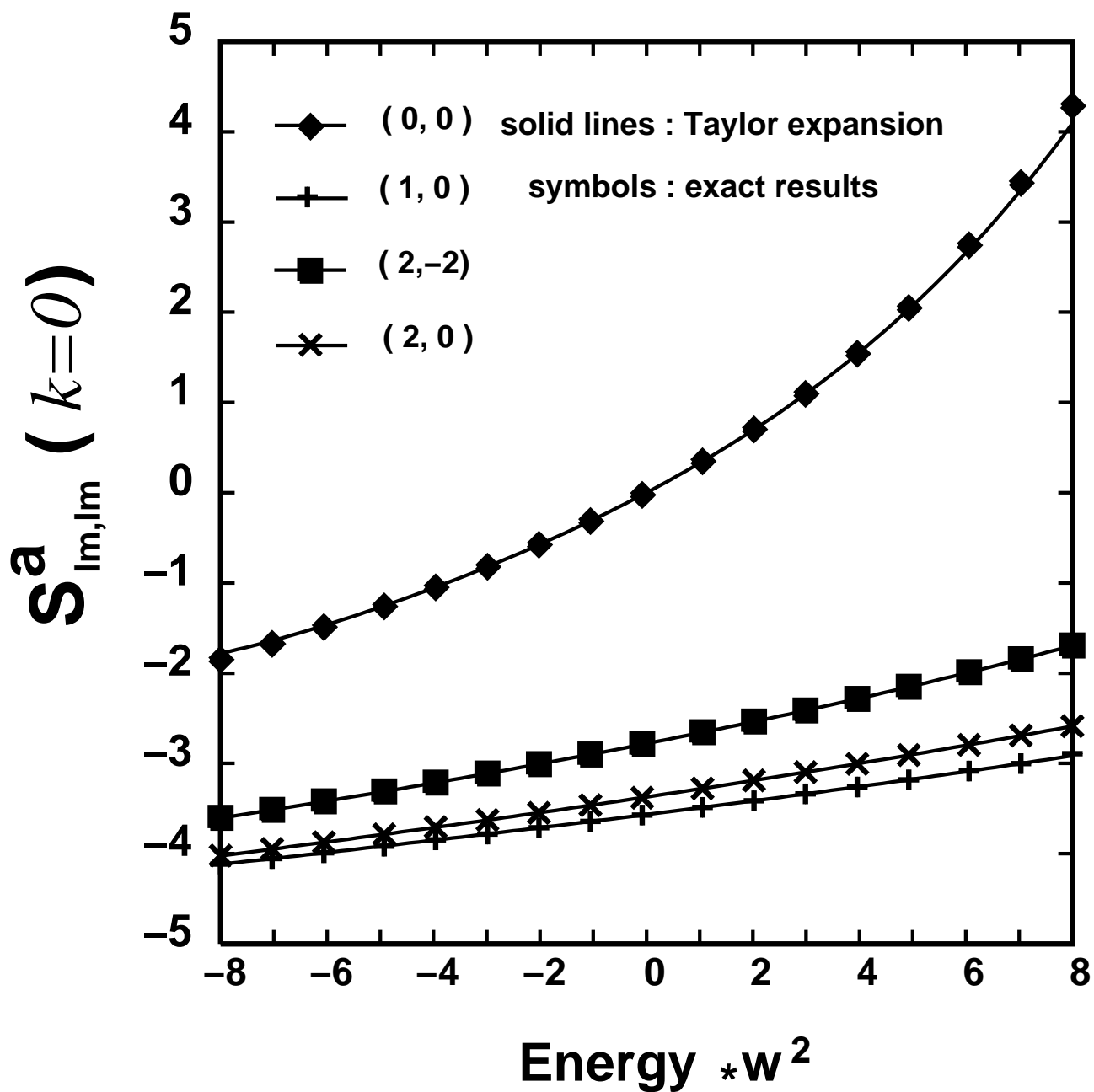
FIG. 5. Charge density contour plots for Al_3Li in $L1_2$ structure and *fcc* Al in units of $0.01 \text{ electrons}/\text{Bohr}^3$ obtained as the output of a self-consistent SCA-EMTO calculations.

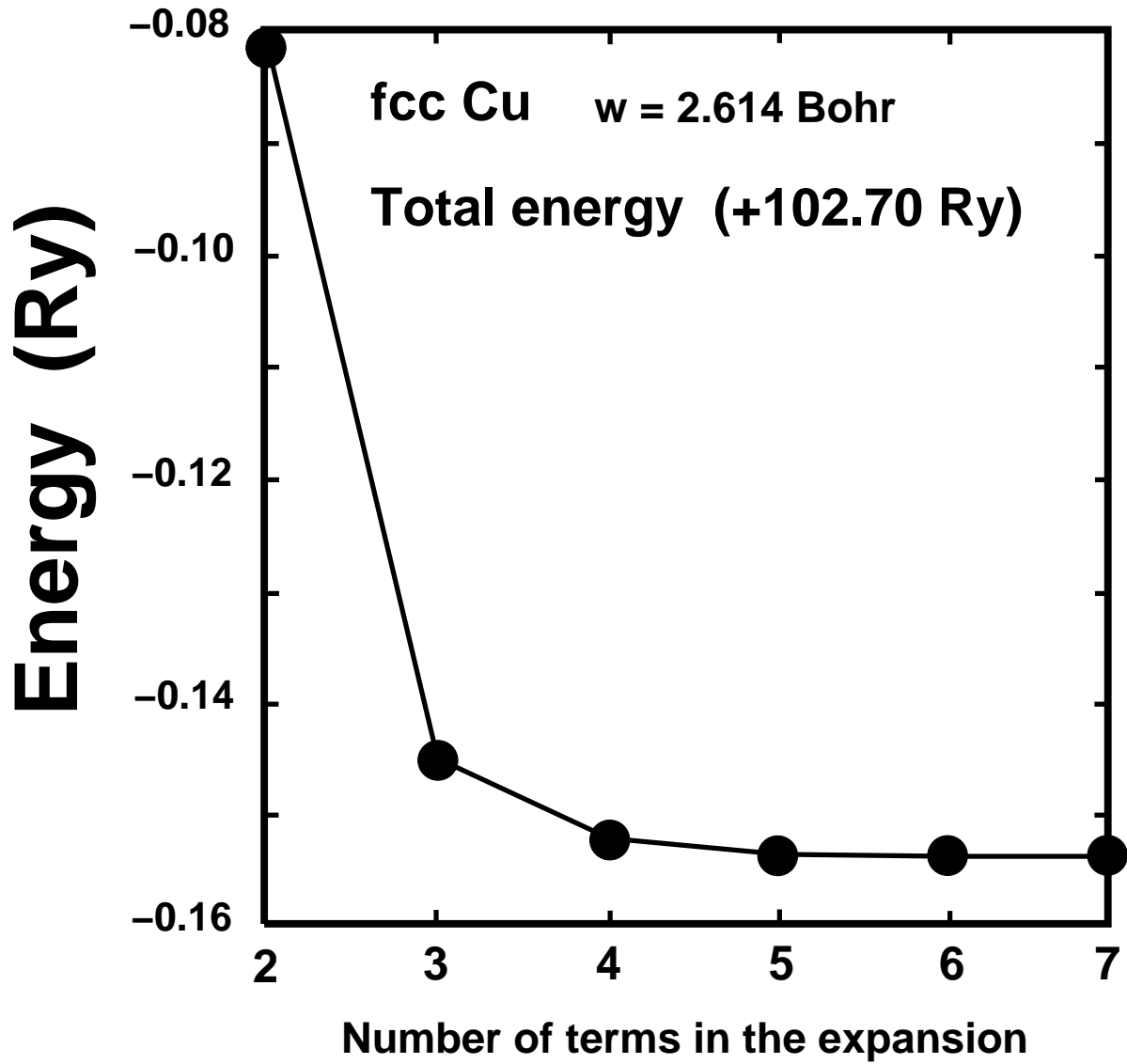
FIG. 6. The change of the atomic radii of the ordered AlLi compounds relative to the radius of the *fcc* Al. The open symbols show the results obtained by the full-potential FLAPW calculation from Ref. [20]. The present SCA-EMTO results are shown by closed symbols. The lines connect the results for the *fcc*-based structures.

FIG. 7. The theoretical bulk moduli for the ordered AlLi compounds. For the notation see caption of Fig. 6.

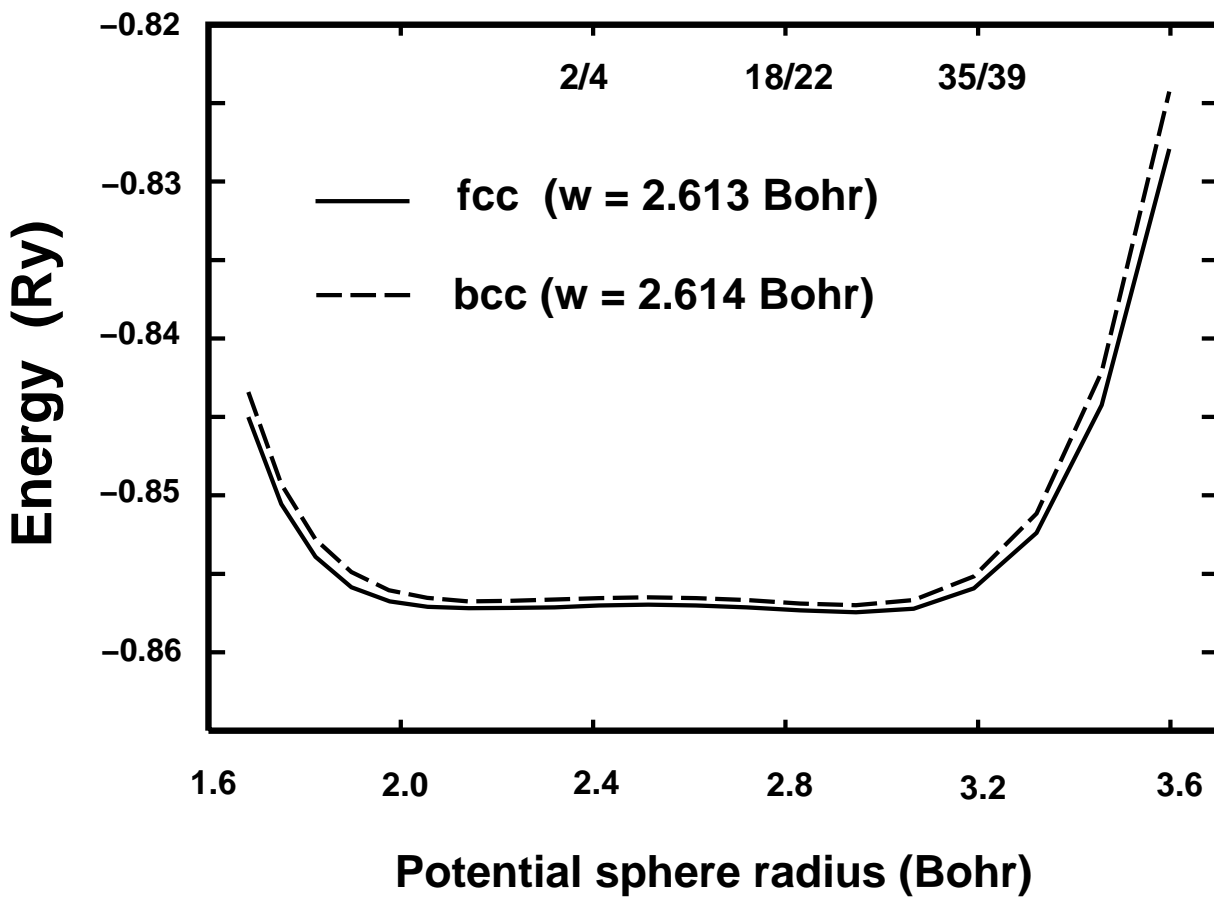
FIG. 8. The theoretical heat of formations for the ordered AlLi compounds. For the pure Al and Li the *fcc*-*bcc* structure energy difference is shown. For the notation see caption of Fig. 6.



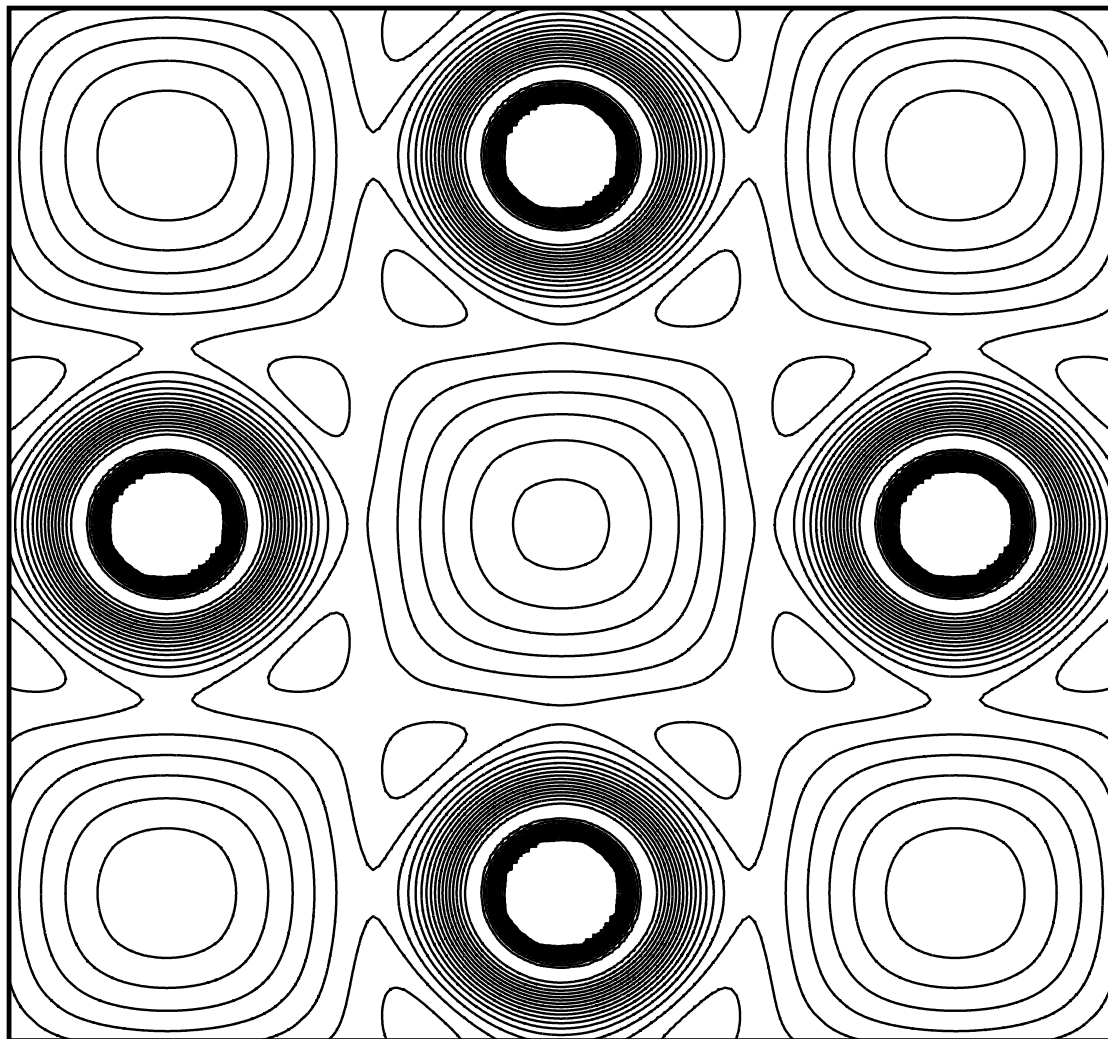




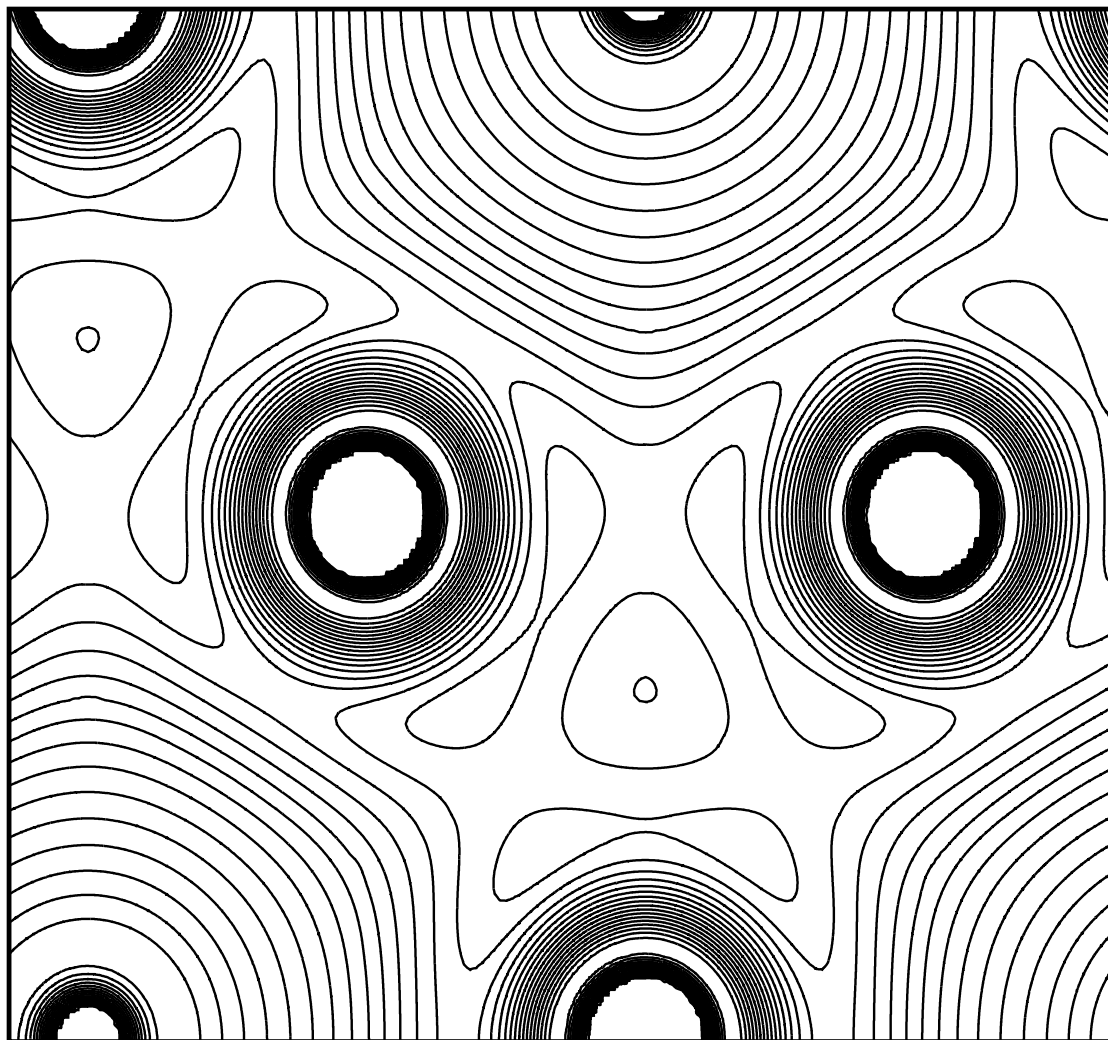
Linear overlap, fcc/bcc (%)



(a) Al₃Li (100)



(b) Al₃Li (111)



(c) Al (111)

